

We are IntechOpen, the world's leading publisher of Open Access books Built by scientists, for scientists

6,900

Open access books available

186,000

International authors and editors

200M

Downloads

Our authors are among the

154

Countries delivered to

TOP 1%

most cited scientists

12.2%

Contributors from top 500 universities



WEB OF SCIENCE™

Selection of our books indexed in the Book Citation Index
in Web of Science™ Core Collection (BKCI)

Interested in publishing with us?
Contact book.department@intechopen.com

Numbers displayed above are based on latest data collected.
For more information visit www.intechopen.com



Microwave Imaging for Early Breast Cancer Detection

Yoshihiko Kuwahara

Additional information is available at the end of the chapter

<http://dx.doi.org/10.5772/intechopen.69562>

Abstract

We overview the research trend on microwave imaging for early breast cancer detection. The technologies have two categories: ultra-wide band (UWB) radar that reconstructs the scattering power distribution in the breast and inverse scattering problem that reconstructs the dielectric properties distribution. We have developed a clinical equipment using UWB radar and carried out clinical test 4 years ago. Through the experiments, we concluded that the UWB radar was insufficient for the clinical equipment, because the UWB radar cannot discriminate cancerous tumor and other lesions. Therefore, we have been studying inverse scattering. It is a challenging task to develop an equipment using inverse scattering technologies. We have proposed a microwave mammography that has four features: (1) sensor with breast fixing by absorption, (2) small sensor with multipolarization, (3) image reconstruction program linking the commercial EM simulator, and (4) hybrid imaging method using UWB radar and inverse scattering.

Keywords: early breast cancer detection, microwave imaging, radar, inverse scattering, hybrid imaging

1. Introduction

Early detection and treatment of breast cancer, which has the highest rate of incidence in women, are important. Although X-ray mammography is widely used, it has the disadvantages of X-ray exposure, detection failure owing to low contrast, and pain during inspection. An echograph is a well-established alternative to X-ray mammography. However, the inspection quality of this device depends on the skill of the inspector, and the reproducibility of results is poor [1]. Recently, microwave imaging for breast cancer detection has attracted attention [2]. However, the low contrast between fibroglandular tissue and malignant tissue in the microwave frequency range poses a challenge to many researchers [3].

Breast cancer detection through microwave imaging is broadly grouped into two categories: tomography [4] and ultra-wide bandwidth (UWB) radar [5]. Tomography can reconstruct such

organization structures as fatty, fibroglandular, and malignant tissues. However, the electromagnetic analysis including the antennas, supporting structure, and environment must be accurately carried out because measuring error, noise, and modeling error significantly affect the image reconstruction. Moreover, since the calculation load is enormous, it is unsuitable for mass examination. UWB radar cannot reconstruct the organization structure accurately [6]. However, since it is tolerant to measuring error and noise in comparison with tomography, it is easy to manufacture. Furthermore, since the calculation load is small, it is suitable for mass examination.

We have developed multistatic UWB radar for early breast cancer detection. Our equipment features multistatic microwave imaging via space time (MS-MIST) algorithm, which extends the MIST algorithm to multistatic UWB radar [5] and a conformal array, which fixes the breast to the inner shape of a sensor via suction [7]. Through numerical simulations and experiments with phantoms, MS-MIST was confirmed to have high resolution with low artifacts. In addition, our sensor requires neither placement of the breast in a tank filled with a coupling liquid nor measurement of the breast shape. The proposed system has low failure rate of inspection in comparison with the already developed UWB radar [6] because the sensor with suction and fixation restrains the patient from moving and breathing during the scan. Moreover, the inspection time is short because the number of antennas is reduced by MS-MIST with high resolution and low artifact. Hence, it results in small size and low cost. First, we describe the clinical equipment developed and demonstrate the imaging results, including numerical and clinical experiments.

The clinical test results demonstrate that the system can detect cancer that has a clear boundary and is isolated from the fibroglandular tissue. However, if the boundary is irregular or if the tumor is buried under the fibroglandular tissue, the system is unable to correctly reconstruct the shape of the tumor [6]. Therefore, we are currently working on the development of microwave tomography [8–11].

In order to achieve accurate image reconstruction, it is necessary to obtain diverse observation data. Several methods can be employed to obtain diverse observation data. More observation data can be obtained by increasing the number of antennas; however, the scale of the apparatus increases and the computational cost becomes substantial. Furthermore, the signal-to-noise ratio (SNR) is degraded by increasing the size, which degrades the image reconstruction. A method using multiple frequencies has been proposed [12]. In general, biological tissue is a medium with frequency dependence, and its behavior is modeled using the Debye approximation with several parameters. Consequently, the number of unknown parameters increases with the number of frequencies; thus, the reconstruction becomes difficult.

The multiple-polarization method has been examined as a means to obtain a variety of observation data. The impact of polarization on image reconstruction was evaluated in Ref. [13], and it was concluded that the effectiveness was limited. However, the physical considerations related to antenna arrangement have not yet been investigated. Second, we review a compact-sized imaging sensor using multipolarization. We use the distorted Born iterative method (DBIM) described in Ref. [12] to solve the inverse scattering problem.

Microwave tomography can reconstruct complex structures if the measurement system is modeled completely and there is no measurement error. In order to reduce the modeling error, an image-reconstructing program that solves the forward problem using a commercial electromagnetic simulator has been developed [9]. Considering the actual device, this program includes an algorithm that applies the scattering parameters provided by the vector network analyzer (VNA) to the inverse scattering equation [10]. Third, we present microwave mammography with these technologies.

We could successfully reconstruct the complex numerical breast phantom using the proposed microwave mammography. Subsequently, we developed simple microwave tomography and carried out experiments. However, we could not reconstruct a sufficiently high-quality image owing to the deviations between the calculated and measured backscattered signals. It is well known that the settings of the initial complex permittivity distribution are important. Previously, initial permittivity in the imaging area was set to be uniform. Finally, we propose a method in which the backscattered power distribution is reconstructed by the radar, and the distribution is subsequently used as the prior knowledge in the inverse scattering problem. The effectiveness of the proposed method is confirmed by experiments.

2. Breast model and propagation analysis

2.1. Electromagnetic property of the breast

The breast cancer detection based on microwave imaging relies on large differences in the electromagnetic properties between normal and malignant tissues. In quantitative microwave imaging, considering the biological tissues as dielectrics, the dielectric properties are reconstructed according to the differences in the complex permittivity, defined by Eq. (1):

$$\varepsilon^* = \varepsilon_r + j \frac{\sigma}{\omega \varepsilon_0} \quad (1)$$

where ε_r is the relative permittivity, σ is the conductivity of examined object, ε_0 is the free-space permittivity, and ω is the angular frequency.

The electromagnetic properties of breast tissue in different frequency ranges have been studied. Gabriel et al. conducted a major review of measured dielectric properties on healthy human tissues for frequencies between 10 Hz and 100 GHz [14]. In the study, the basic and well-known Debye model in Eq. (2) is introduced:

$$\varepsilon^*(\omega) = \varepsilon_\infty + \frac{\varepsilon_s - \varepsilon_\infty}{1 + j\omega\tau} \quad (2)$$

This equation is extended to the Cole-Cole expression to model the structure and composition of biological tissues, defined in Eq. (3):

$$\varepsilon^*(\omega) = \varepsilon_\infty + \frac{\Delta\varepsilon}{1 + j\omega\tau} + \frac{\sigma_s}{j\omega\varepsilon_0} \quad (3)$$

where ε_∞ is the static frequency permittivity constants, and σ_s is the static conductivity. The magnitude of dispersion is $\Delta\varepsilon = \varepsilon_s - \varepsilon_\infty$. The relaxation time constant τ is assumed to be spatially invariant and usually considered to be in the range of 15–17 ps.

Furthermore, female breast tissues have been studied with focus on breast tumor detection. *Ex vivo* measurements of fresh human malignant and normal breast tissues have been performed by several groups. Lazebnik et al. reported the most comprehensive examination of the dielectric properties of normal, benign, and malignant breast tissues [3].

2.2. Electromagnetic analysis

Microwave mammography consists of multiple antennas placed around the breast as shown in **Figure 1**. An antenna is selected, and subsequently, a microwave signal is transmitted. At this time, the signals received by other antennas are collected. The transmitting antennas are sequentially selected to obtain the received data. We reconstruct the image using a set of received data. In tomography, this physical phenomenon is modeled using a computer. Since the electric constant distribution of the image area is unknown, it is initialized with an appropriate value and repeatedly updated using Newton's method. It is necessary to obtain the electromagnetic field distribution of the image area to apply the Newton's method.

Several methods can be used to solve the electromagnetic problem, including the method of moment (MoM), finite element (FEM), and finite-difference time-domain (FDTD) [15]. It is a very difficult task to prepare the original program using these methods.

In recent years, many commercial electromagnetic field analysis simulators have been developed and widely used for antenna design, electromagnetic compatibility analysis, etc. Commercial simulators are well debugged, and various methods for modeling with high accuracy are adopted. Many simulators have functions to link with external software. We linked

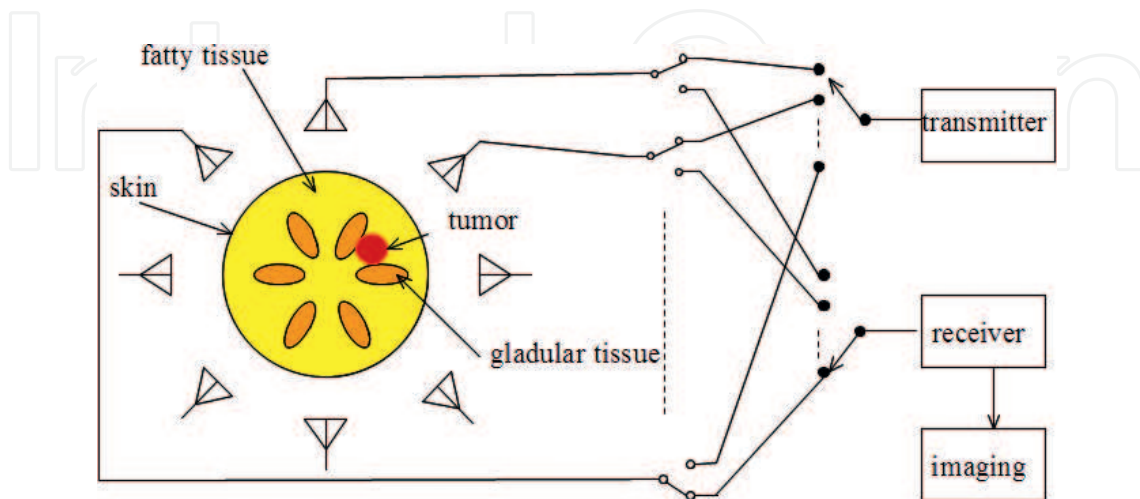


Figure 1. Breast screening by microwave imaging.

MATLAB with simulators such as FEMTET, MW-S, and HFSS, analyzed the electromagnetic field with a simulator, and reconstructed the image using the MATLAB program. If the modeling error is disregarded, electromagnetic field analysis using the FDTD method or MoM is possible.

3. Image reconstruction algorithm

In this section, we overview the image reconstruction algorithm using a microwave signal.

3.1. UWB radar

Ultra-wide band (UWB) radar reconstructs the backscattered power distribution in the breast. The image does not accurately reflect the tissue structure of the breast. However, it may be possible to detect the presence or absence of abnormality such as cancer and its position. Recently, new findings such as adaptive beamforming, utilization of the symmetrical structure of left and right breasts, combined use of magnetic nanoparticles, etc. have been proposed. These proposals can be powerful tools for UWB radar.

3.1.1. Delay and sum

Figure 2 shows the principle of imaging by delay and sum. Consider a scatterer in the imaging area and an array antenna around it. We set a focal point in the imaging area and assume there is a scatterer at that position. When a pulse is transmitted from one antenna and received by the same antenna, the arrival time of the reflected waveform is delayed for the antenna away from the scatterer. Assuming that the distance from the receiving antenna to the transmitting antenna via the focal length is l and the propagation velocity of the wave is v , the time required for the radio waves emitted from the transmitting antenna to arrive at the receiving antenna is $t = l/v$ [s]. When calculating the arrival time required for each antenna and advancing the time response by that amount, if there is a scatterer in the focal point, a coherent time response is obtained and a large response can be obtained by summing. If there are no scatterers in the focus, a large response cannot be obtained even after summing. Subsequently, the focal point is moved within the imaging area, the time response is reversed, and the distribution map is created. The power will be large at the position where the scatterer is present, and it becomes small at the position where the scatterer is absent. This is the same as the imaging principle of the ultrasonic diagnostic apparatus. In this scheme, a narrow pulse with wideband is used to enhance the resolution. Moreover, the algorithm can be easily extended to multistatic radars with different receiving and transmitting antennas.

3.1.2. Microwave imaging via space time

In microwave imaging via space time (MIST) beamforming for wideband monostatic radar [16], the beamformer weights that adjust the array gain at a set focal position in a unit are determined by the least mean square scheme. The transmitting and receiving antennas are identical. In our approach, several receiving antennas are used. Robust and clear images can be expected because

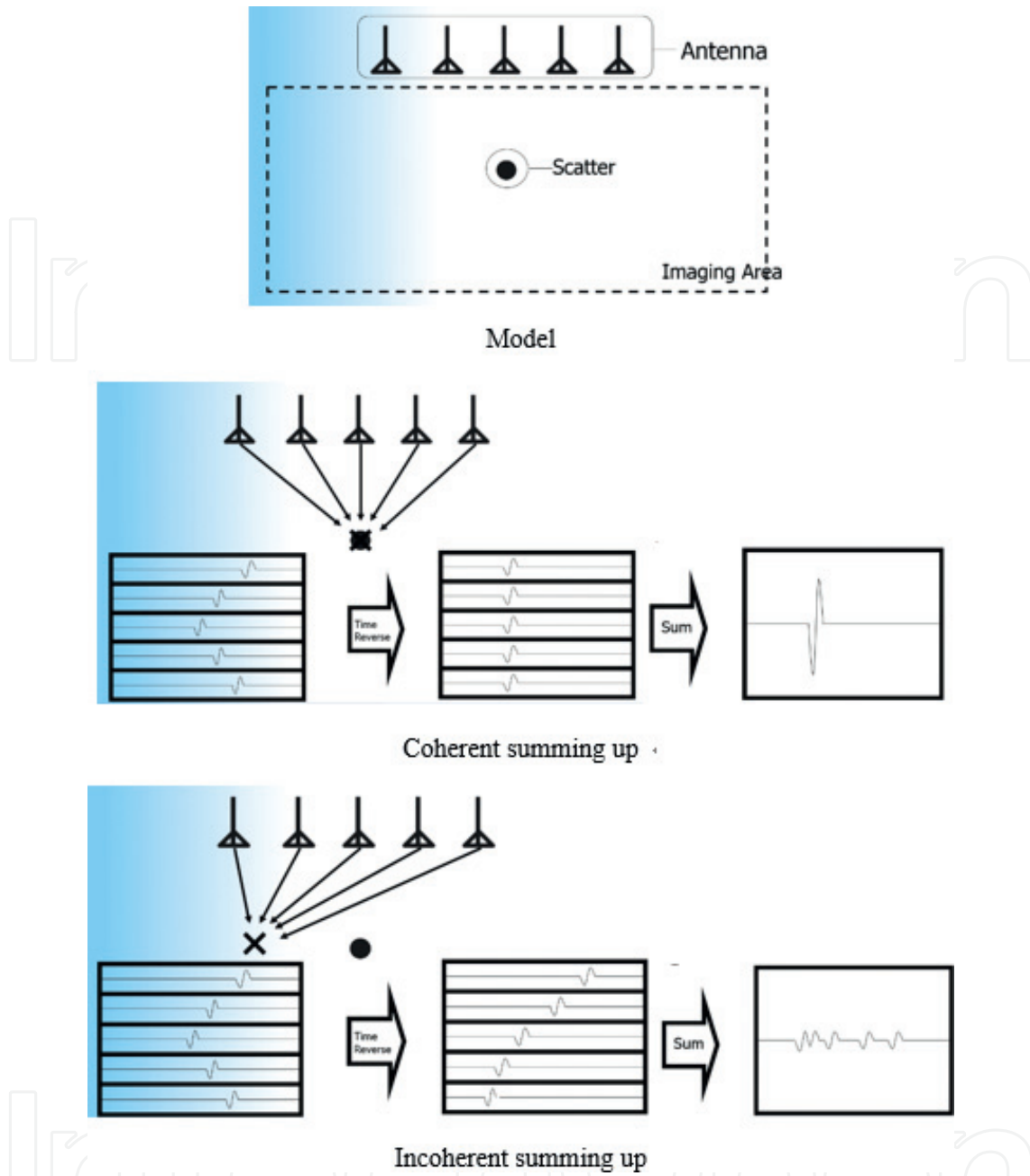


Figure 2. Delay-and-sum.

the scattered response from the tumor enhances the contrast. By computing the output power distribution of the beamformer over the imaging area, a three-dimensional image of backscattered power is reconstructed. The tumor can be detected because a large amount of scattering occurs around it. The weight of the conventional MIST beamformer is expressed by the following formula:

$$W_i(l) = \frac{I(\omega_l) \hat{S}_{ii}(\mathbf{r}_0, \omega_l) e^{j\omega_l \tau_0 T_s}}{|I(\omega_l) \hat{S}_{ii}(\mathbf{r}_0, \omega_l)| \{1 + |I(\omega_l)| \sum_{i=1}^M \hat{S}_{ii}(\mathbf{r}_0, \omega_l)\}} \quad (4)$$

where $I(\omega_l)$, $\hat{S}_{ii}(\mathbf{r}_0, \omega_l)$, τ_0 , T_s , and M denote the spectral component of the transmitting signal at frequency ω_l , monostatic radar response of the i th antenna at position \mathbf{r}_0 , excluding the phase shifts owing to the propagation delays, average propagation delay of the beamformer, sampling period, and number of elements, respectively. The weight of the proposed beamformer is expressed by the following formula:

$$W_{ij}(l) = \frac{I(\omega_l) \hat{S}_{ij}(\mathbf{r}_0, \omega_l) e^{j\omega_l \tau_0 T_s}}{|I(\omega_l) \hat{S}_{ij}(\mathbf{r}_0, \omega_l)| \{1 + |I(\omega_l)| \sum_{i=1}^M \sum_{j=1}^M \hat{S}_{ij}(\mathbf{r}_0, \omega_l)\}} \quad (5)$$

where $\hat{S}_{ij}(\mathbf{r}_0, \omega_l)$ is the multistatic radar response at position \mathbf{r}_0 , excluding the phase shifts owing to the propagation delays when the i th and j th antennas are used as the transmitting and receiving antennas, respectively.

3.2. Inverse scattering (microwave tomography)

3.2.1. Theory

Figure 3 shows the flow of image reconstruction with the inverse scattering problem. First, E_{meas}^s , i.e., the measured data for all the combinations of transmitting and receiving antennas are collected. On the other hand, the contrast based on electric properties is initialized in C_0 in the work station. Based on the current contrast, E_{calc}^s , i.e., calculated data for all the combinations are estimated. Simultaneously, Jacobian, i.e., the sensitivity matrix J is also calculated based on

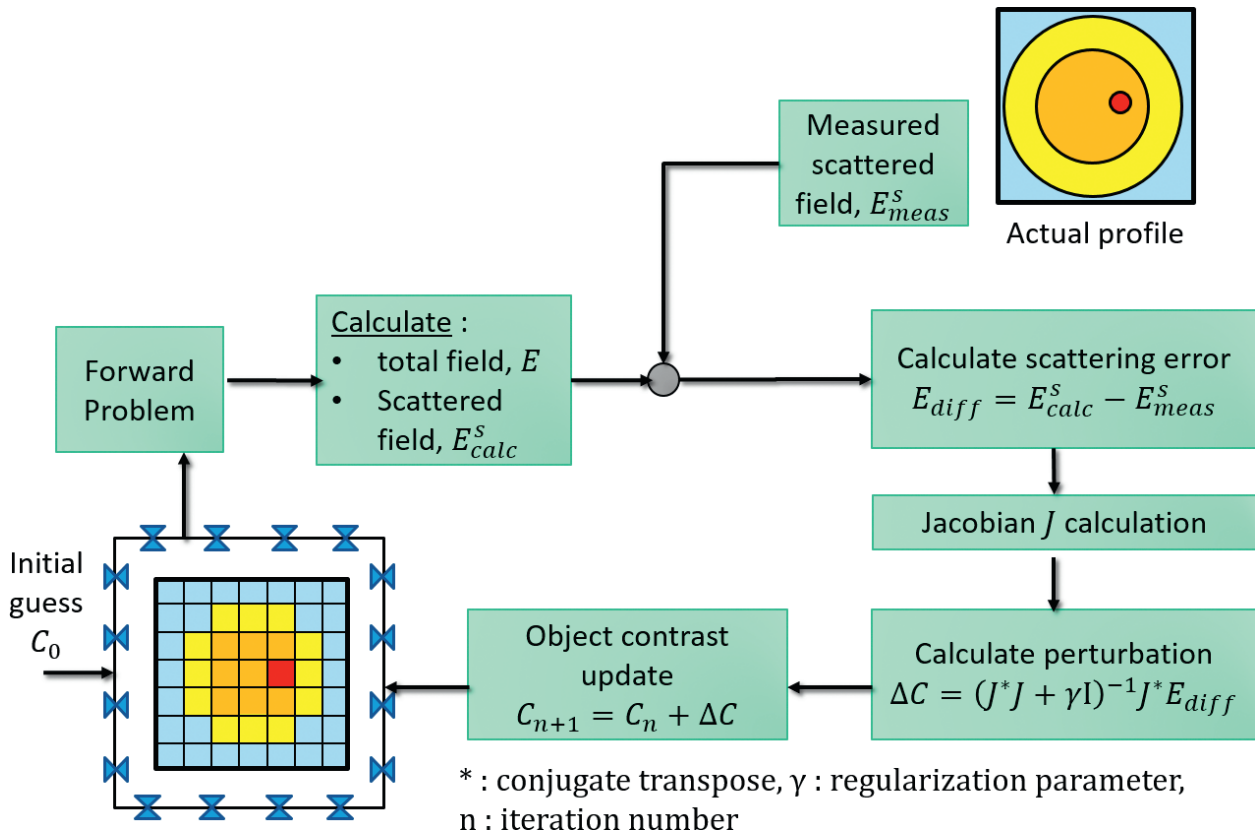


Figure 3. Inverse scattering problem.

the total field in the imaging area E . After calculating perturbation of the contrast ΔC , the contrast is renewed.

3.2.2. Distorted born iterative method

In the DBIM, the relationship between the relative permittivity ε , conductivity σ , and scattering field e^s is expressed as follows [12]

$$\begin{bmatrix} R_e(e^s) \\ I_m(e^s) \end{bmatrix} = \begin{bmatrix} R_e \left\{ \frac{\partial F}{\partial \varepsilon} \mathbf{B} \frac{\partial F}{\partial \sigma} \mathbf{B} \right\} \\ I_m \left\{ \frac{\partial F}{\partial \varepsilon} \mathbf{B} \frac{\partial F}{\partial \sigma} \mathbf{B} \right\} \end{bmatrix} \begin{bmatrix} \varepsilon_1 - \varepsilon_1^b \\ \vdots \\ \varepsilon_K - \varepsilon_K^b \\ \sigma_1 - \sigma_1^b \\ \vdots \\ \sigma_K - \sigma_K^b \end{bmatrix} \quad (6)$$

$$\mathbf{B} = \left[\mathbf{H}_{1,1}^T \mathbf{H}_{1,2}^T \dots \mathbf{H}_{M,N}^T \right]^T \quad \mathbf{F} = \varepsilon + \frac{\sigma}{j\omega\varepsilon_0}$$

$$\mathbf{H}_{m,n} = \left[\overline{\mathbf{G}}^b(\mathbf{r}_n|\mathbf{v}_1) \mathbf{E}^b(\mathbf{v}_1|\mathbf{r}_m) \dots \overline{\mathbf{G}}^b(\mathbf{r}_n|\mathbf{v}_K) \mathbf{E}^b(\mathbf{v}_K|\mathbf{r}_m) \right] \in \mathbb{C}^{3 \times K}$$

$$m = 1, \dots, M, \quad n = 1, \dots, N$$

In Eq. (6), $R_e(\cdot)$ and $I_m(\cdot)$ denote the real part and imaginary part, respectively. Further, ε^b and σ^b denote the relative permittivity and conductivity in the background, respectively. K is the number of discretized voxels in the breast region, and M and N are the number of transmitters and receivers, respectively. F is the complex relative permittivity. $\overline{\mathbf{G}}^b(\mathbf{r}_n|\mathbf{v}_k)$ is the dyadic Green's function for the n th receiver at position \mathbf{r}_n and the k th voxel at position \mathbf{v}_k . $\mathbf{E}^b(\mathbf{v}_k|\mathbf{r}_m)$ is the background electric field at \mathbf{v}_k when the m th transmitter is used.

Eq. (6) is transformed to the normal equation, and subsequently, Tikhonov regularization is applied, because Eq. (6) is ill posed in general. We solve Eq. (6) and obtain the solutions $\Delta\varepsilon_k = \varepsilon_k - \varepsilon_k^b$ and $\Delta\sigma_k = \sigma_k - \sigma_k^b$. Subsequently, we update the relative permittivity and conductivity using the solutions as follows:

$$\varepsilon_{k+1} = \varepsilon_k + \Delta\varepsilon_k \quad \sigma_{k+1} = \sigma_k + \Delta\sigma_k \quad (7)$$

The DBIM iterates the aforementioned procedure until the terminating conditions are satisfied.

4. Development and clinical test of UWB radar

In this section, we demonstrate the development and clinical test of UWB radar.

4.1. System configuration

A schematic diagram and photographs of the developed microwave mammography equipment are shown in **Figure 4**. The equipment comprises a sensor, aspirator, antenna switch, network analyzer, PC for control, and workstation (WS) for data processing.

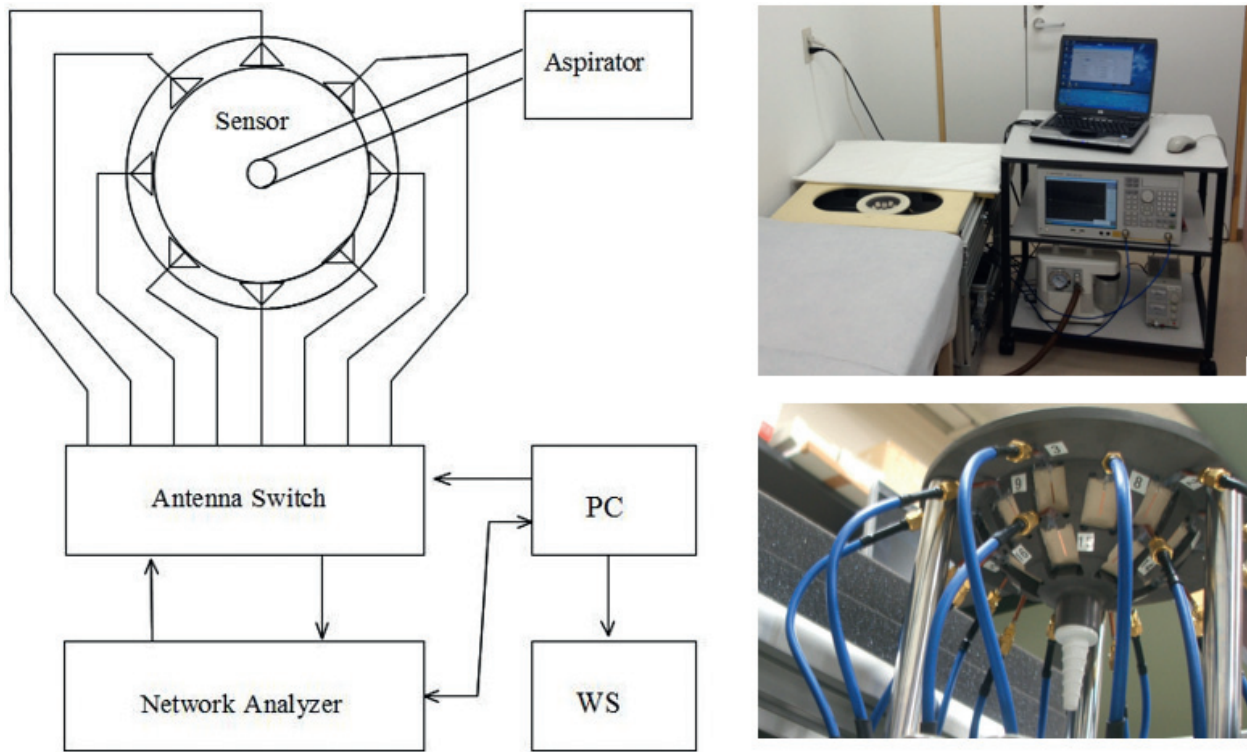


Figure 4. Microwave mammography.

4.2. Sensor

Figure 5 shows the concept of the proposed sensor. It consists of several stacked patch antennas fed by the slot. The number of antennas depends on the breast size. The antennas are embedded in a cup manufactured by Sumitomo Electric Industries, Ltd., whose material has almost the same electromagnetic parameters as the adipose tissue ($\epsilon_r = 6.3$, $\sigma = 0.15$, at 6 GHz). The elements are designed in order to match impedance over the bandwidth of 4–9 GHz when the aperture

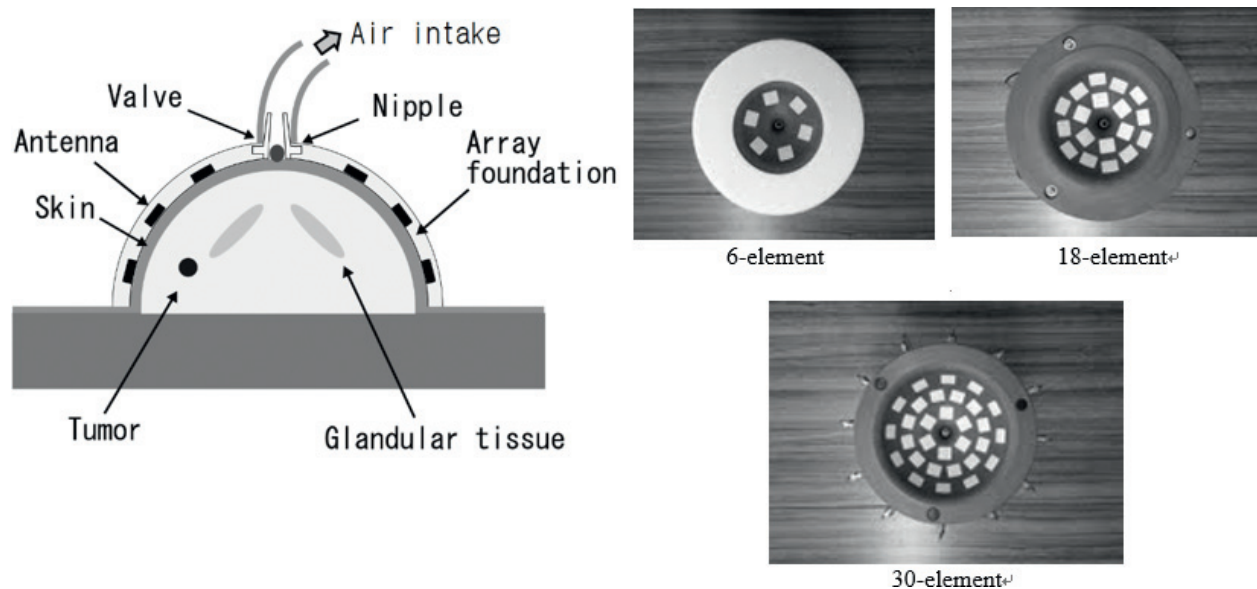


Figure 5. Sensor.

touches the breast. When the pressure in the sensor is reduced by the aspirator, the breast is fixed to the inside of the sensor. Therefore, we need not know the breast shape for the image reconstruction process.

As shown in **Figure 5**, we prepared three different sensor types for various breast sizes: a 30-element sensor with a diameter of 13 cm and a depth of 5.4 cm (large), a 18-element sensor with a diameter of 10 cm and a depth of 4 cm (medium), and a 6-element sensor with a diameter of 8 cm and a depth of 2 cm (small).

4.3. Antenna switch and control

The antenna switch selects one or two antennas connected to the input/output port of the network analyzer (Agilent E5071C) and can correspond with the three sensor types. It consists of 42 single-port double-transfer (SPDT) switches and 6 single-port 6-transfer (SP6T) switches. The total insertion loss is less than 5 dB at 6.5 GHz, and the peak amplitude and phase deviation are less than 0.2 dB and 10° , respectively. The antenna switch and network analyzer are automatically controlled by the PC.

4.4. Clinical inspection

The size of the microwave mammography equipment is 600 (width) \times 600 (length) \times 500 (height) mm. It is designed to align and connect lengthwise with a bed in the consulting room. Before inspection, a sensor of the proper size must be selected. Using a transparent cup with the same size as the sensor on the breast and subsequently by decompressing, one can confirm that the breast touches all the elements by observation. Subsequently, the patient lies face down on the bed and places her breast in the sensor and suction begins. The value of S_{11} when the breast is placed in the sensor is compared with the value of S_{11} when no breast is present. If S_{11} is not sufficiently reduced, an alarm is activated. In this case, the inspector aligns the position or inclination of the sensor. The inspection time is approximately 5, 30, and 200 s for 6, 18, and 30 sensor elements, respectively. An array rotation technique is used for artifact removal [5]. Additional inspection when the sensor is mechanically rotated by 20° is carried out.

4.5. Imaging results

4.5.1. Early breast cancer in fatty breast tissue

We imaged the breasts of an elderly woman with fatty tissue. Referring to the magnetic resonant imaging (MRI) image shown in **Figure 6**, her right breast is infected with early breast cancer with a tumor that is 9 mm in diameter at the lower inside near the chest wall, whereas no pathological changes can be seen in her left breast. In this case, the boundary of the tumor is comparatively clear, and it is isolated from the fibroglandular tissue.

Figure 6 shows the imaging results using microwave mammography. In this case, a small-sized sensor was used. The reflection strength is normalized by the peak reflection field where it is generated around the cancer. Subsequently, areas where the backscattered energy is more than 80% of the peak scattered power are shown. In addition, the estimated position and size

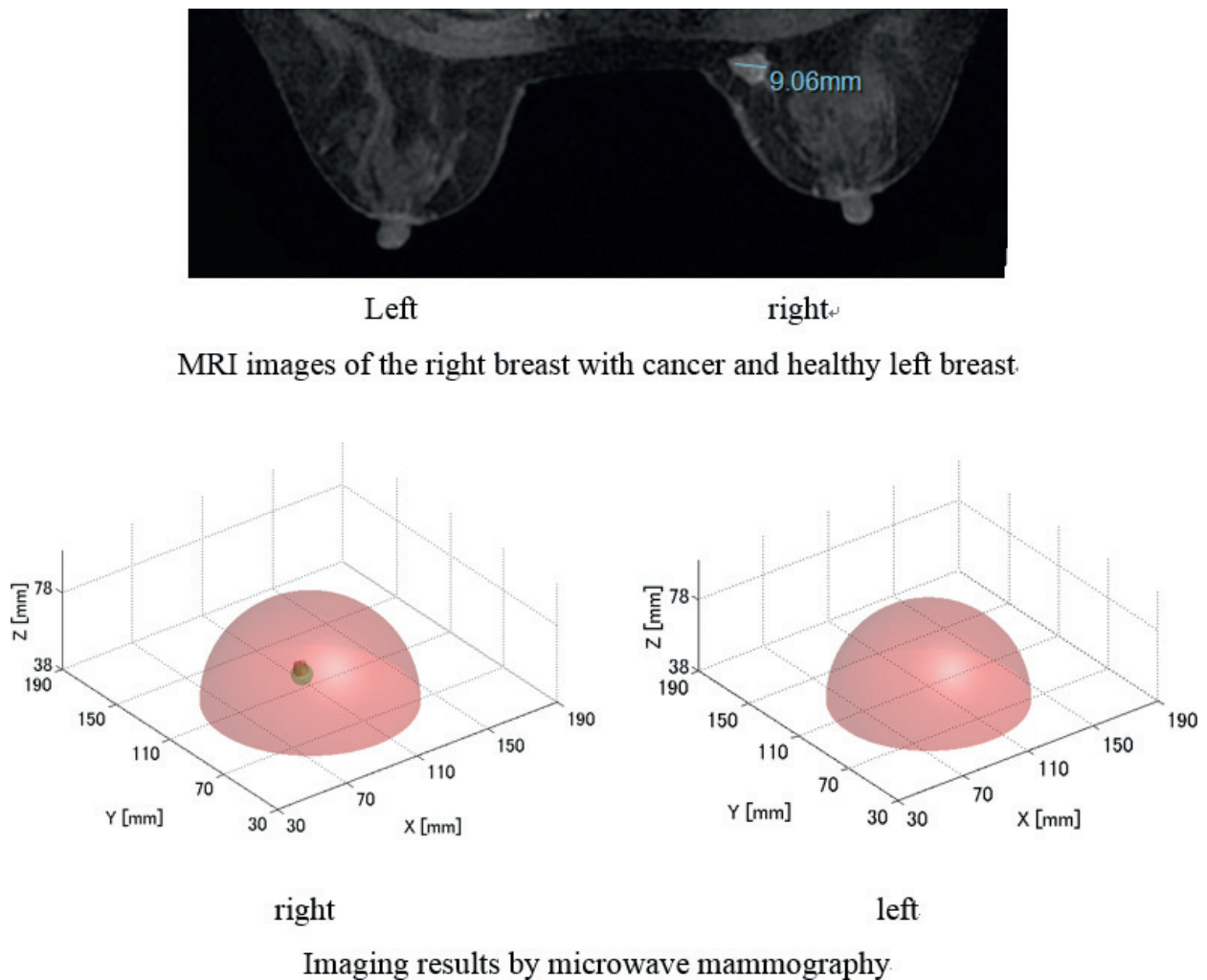


Figure 6. Imaging results: early breast cancer in fatty breast tissue.

from the MRI image are shown with a green circle. These conditions are applied to all the following figures. We can observe a large scattering near the tumor.

4.5.2. Cancerous tumor in rich fibro-glandular tissue

We imaged the breasts of a middle-aged woman with rich fibroglandular tissue. Referring to the MRI Image shown in **Figure 7**, her left breast is infected with a cancerous tumor with a diameter of 1.8 cm at the upper outside near the chest wall. In this case, the boundary is irregular since the cancer is invasive. In addition, it is embedded in the fibroglandular tissue. It is a serious situation for the UWB radar.

Figure 7 shows the imaging results using microwave mammography. In this case, a medium-sized sensor was also used. We can observe a large scattering around the tumor. However, it is difficult to image the outline of the cancerous tumor since the distribution is sparsely dispersive.

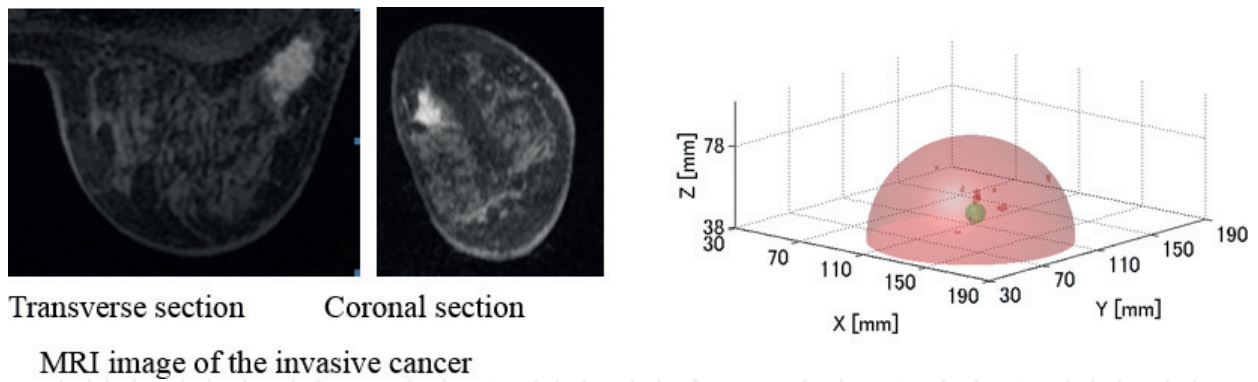


Figure 7. Imaging results: cancerous tumor in rich fibroglandular tissue.

4.6. Discussion

Microwave mammography can detect a cancerous tumor whose boundary is clear and which is isolated from the fibroglandular tissue. On the other hand, it is difficult to detect the cancerous tumor whose boundary is irregular and which is buried in the fibroglandular tissue. In order to overcome the problem, an algorithm to map the complex dielectric constant distribution should be developed by using the inverse scattering problem.

5. Development of microwave tomography

In this section, we describe the key technologies and current status of development of microwave tomography.

5.1. Sensor using multipolarization

In tomography, the breast model is expressed as a set of voxels, and the dielectric properties are estimated in each voxel. The total number of voxels is K , and the dielectric property, which consists of the relative permittivity and conductivity distribution, is represented by the contrast. The calculated data group Y_{mn} , which is based on the estimated model, is compared with the measured data group X_{mn} which is based on the actual model ($m = 1, \dots, N$, $n = 1, \dots, N$, where N is the total number of antennas, m is the number of transmitters, and n is the number of receivers). The contrast (relative permittivity and conductivity) distribution of the breast model is iteratively updated by the DBIM until $X_{mn} \approx Y_{mn}$ is reached.

In the inverse scattering problem, a large amount of diverse observation data is required to achieve accurate image reconstruction with high resolution. In addition, if the measurement error increases owing to low SNR, it cannot reconstruct the image accurately. Therefore, it is better to reduce the analysis region in order to improve the SNR and to reduce the computational cost. When a small sensor is used, a large number of antennas must be arranged in a limited space. In this case, the acquisition of diverse observation data cannot be guaranteed. Subsequently, it is impossible to solve the inverse scattering problem accurately. Nevertheless,

various observation data can be obtained even in a small space by changing the plane of polarization.

5.1.1. Simulation model

Figure 8 shows the aperture of the imaging sensor with dimensions $96 \text{ mm} \times 96 \text{ mm} \times 48 \text{ mm}$ (width \times length \times height). The imaging region is discretized into 1183 voxels to obtain 8-mm resolution. A dipole with a length of 20 mm is used for the antennas, and they are arranged in a 4×2 configuration on each of the four side panels of the sensor. **Figure 8(a)** shows the position of the antenna. The lines in **Figure 8** represent the polarization direction of the antenna, where the y -axis indicates vertical polarization, and the x - or z -axis indicates horizontal polarization. The antenna arrangements at each side are identical. In this study, we investigated three different configurations as shown in **Figure 8** to examine the effectiveness of polarization in breast cancer detection. **Figure 8(a)** illustrates the vertical polarization, **Figure 8(b)** the horizontal polarization, and **Figure 8(c)** the vertical and horizontal polarization (hereafter referred to as multipolarization).

Antennas are buried in the resin. A hemispheric volume is provided inside the sensor to accommodate the breast model, similar to the imaging sensor with fixed suction proposed in Ref. [7]. The simple breast model shown in **Figure 9** consists of adipose tissues, fibroglandular

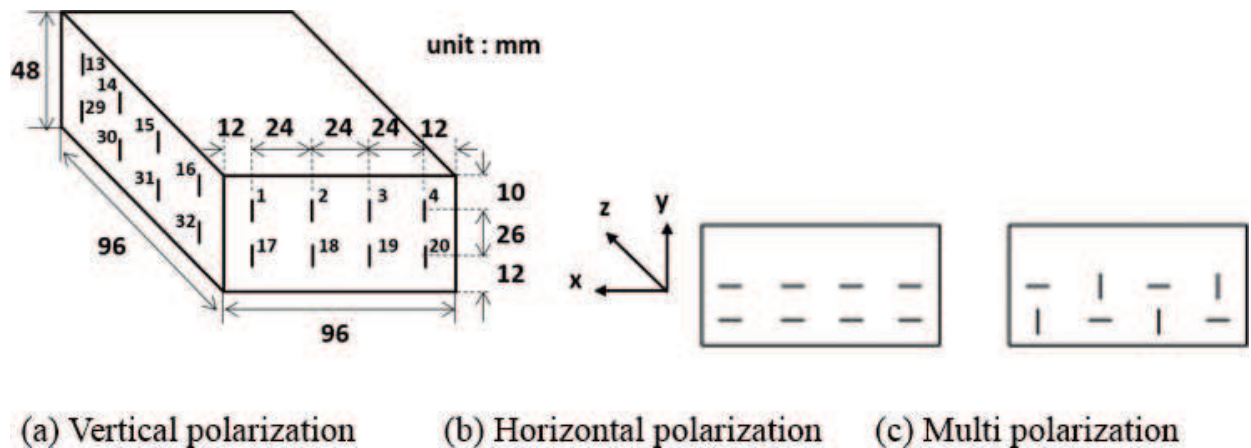


Figure 8. Imaging sensor with various polarizations.

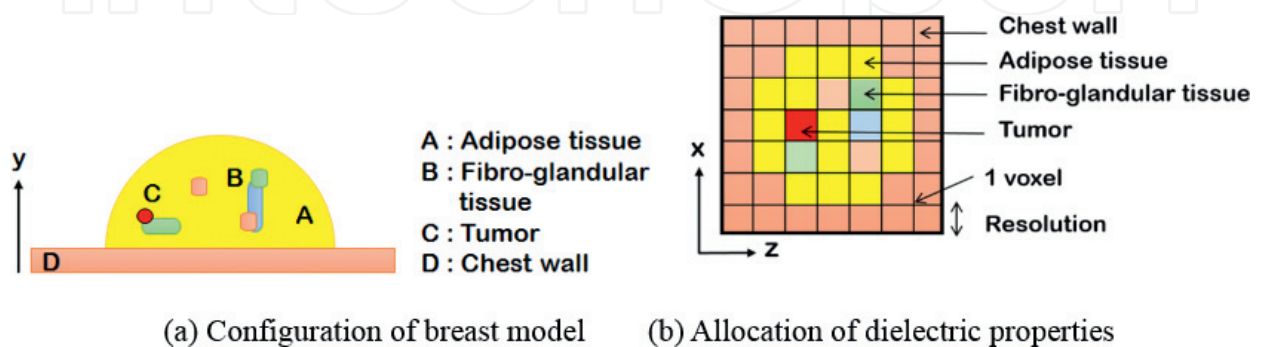


Figure 9. A simple breast model.

| | Relative permittivity, ϵ_r | Conductivity, σ |
|-----------------------|-------------------------------------|------------------------|
| Background | 8 | 0.15 |
| Chest wall | 57 | 2 |
| Adipose tissue | 7 | 0.4 |
| Fibroglandular tissue | 25–10 | 1–2.2 |
| Tumor | 52 | 4 |

Table 1. Dielectric properties of breast model.

tissues, and a tumor. The breast model is a hemisphere with a radius of 48 mm, and the tumor has a radius of 4 mm. The chest wall under the breast is also modeled. Ten percent of the volume ratio of the breast is occupied by fibroglandular tissues. This ratio is the average value measured in Japanese women in their 50s. We characterized the dielectric properties of the breast model in each voxel, as shown in **Table 1**.

5.1.2. Numerical results

The total field within the scattering object was calculated according to the method of moment (MOM) as described in Ref. [15, 17]. Further, we used a single frequency of 2.5 GHz. The analysis region consists of the chest wall, adipose tissue, fibroglandular tissue, and a tumor. Moreover, 10% of the volume ratio is occupied by fibroglandular tissues distributed randomly. The vertical and horizontal cross-section of the two unknown parameters, i.e., the relative permittivity and conductivity are shown in **Figure 10**. The units of the x , y , and z coordinates in the figure are meters. The setting model is shown in **Figure 10(a)**, where the chest wall has been omitted. **Figure 10(b)–(d)** shows the results of reconstruction after 350 iterations, using vertical, horizontal, and multipolarization, respectively, for transmitting and receiving data. From the results, we cannot estimate both the relative permittivity and conductivity of the tumor using single polarization, i.e., vertical and horizontal polarization. In contrast, **Figure 10 (d)** clearly indicates the presence of the tumor, and the reconstruction is successful for both parameters using multipolarization.

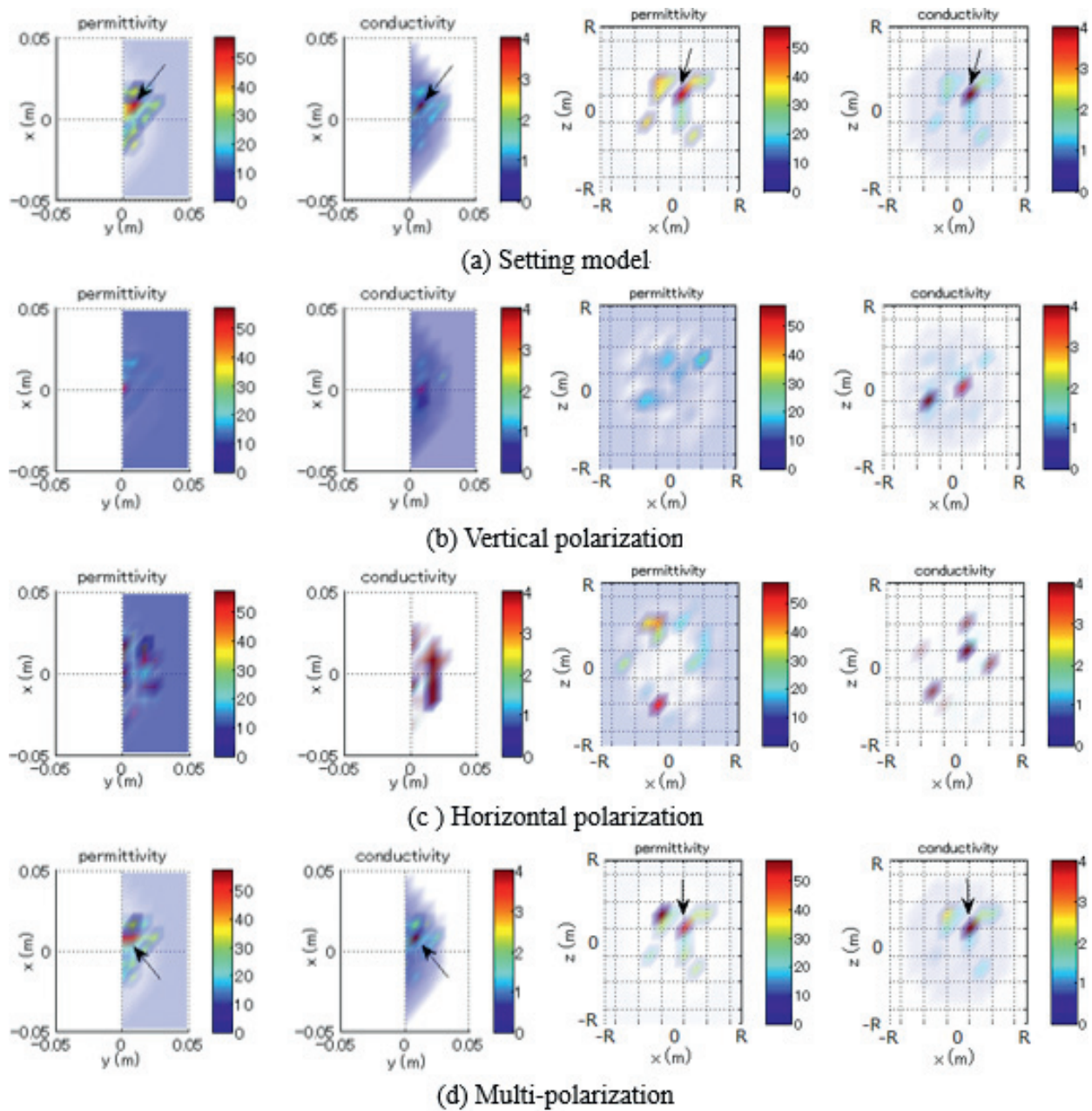
5.1.3. Discussion

We have confirmed the effectiveness of applying multipolarization to transmitting and receiving antennas in order to determine the dielectric property distributions of a simple breast model. The numerical simulation results demonstrate that the ill-posed problem can be avoided by multipolarization.

5.2. Microwave mammography with a small sensor and a commercial electromagnetic simulator

5.2.1. Imaging sensor with polarization diversity

Based on the discussion in Section 5.1, we propose an imaging sensor with multiple polarizations as shown in **Figure 11**. This sensor is a cuboid, and the aperture size is 96 mm \times 96 mm \times



Transverse section

Coronal section

Figure 10. Setting model and reconstructed images after 350 iterations.

48 mm. Six printed dipole antennas are located on each of the four sides, and 12 are located on the top. On each side, the polarization of the antenna changes alternately.

The details of the printed dipole antennas are shown in **Figure 12**. The thickness of the substrate is 0.762 mm, relative permittivity is 10.2, and $\tan \delta$ is 0.0023. In order to simplify the model, the etching patterns are parallel to either of the x , y , or z axes. The dipole antennas are embedded in the dielectric block whose permittivity and conductivity are almost the same as that of adipose tissue. The resonant frequency is 1.8 GHz.

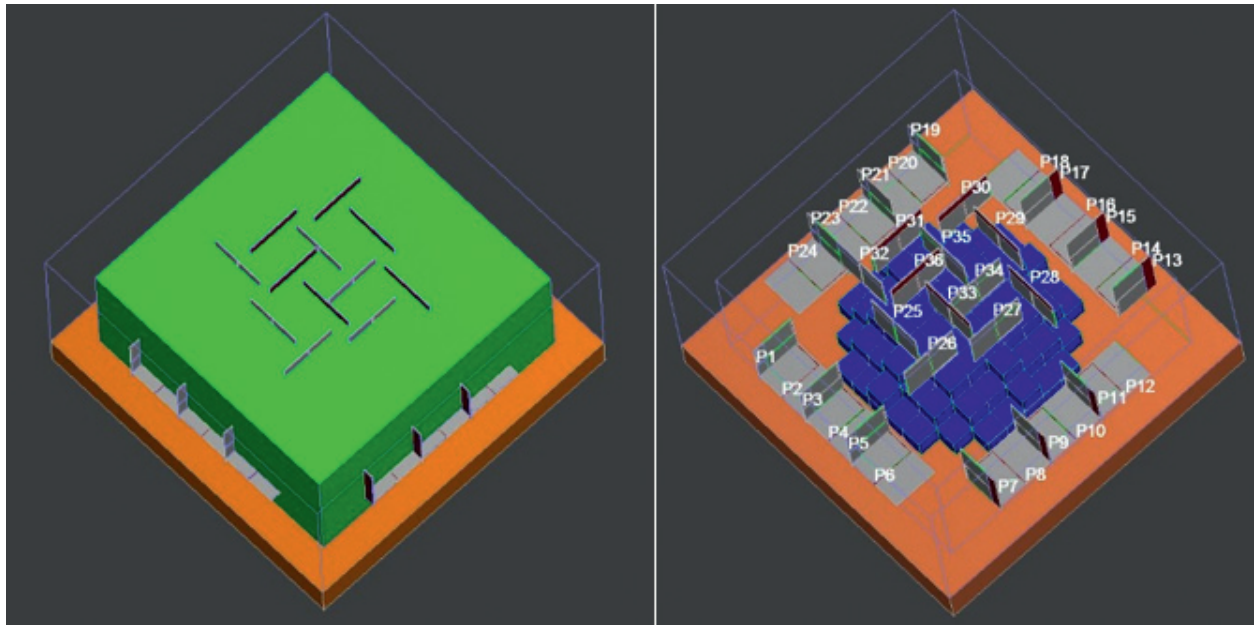


Figure 11. Imaging sensor with polarization diversity.

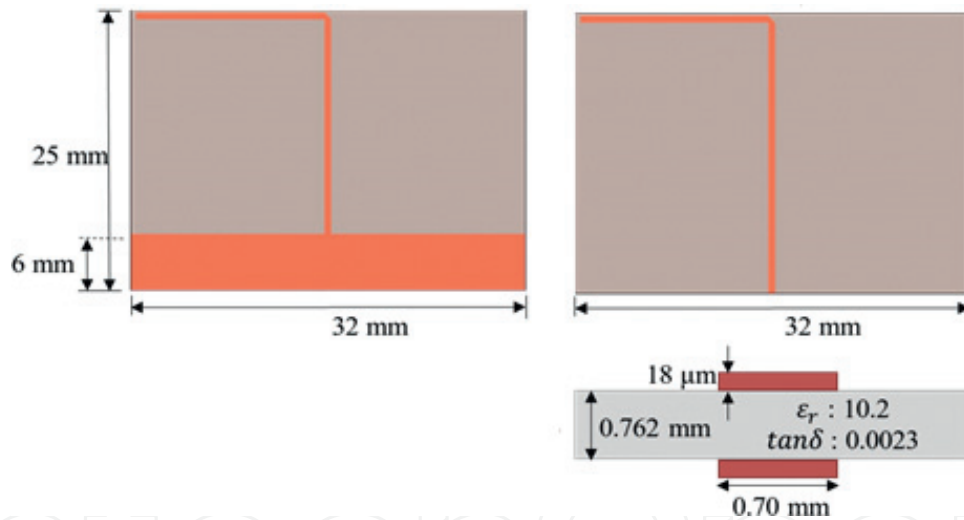


Figure 12. Detail of antenna.

A hemispherical space with a radius of 48 mm and height of 40 mm is prepared for the breast at the bottom of the dielectric block. Furthermore, to absorb the breast, a valve is prepared on the top in order to shape the breast into a hemisphere and to fix the breast to the sensor. With the proposed structure, the breast shape, which is important prior knowledge, can be used in the inverse scattering problems.

5.2.2. Linking with commercial electromagnetic simulator

We can perform electromagnetic analyses with small modeling errors by importing the CAD data of the imaging system into a commercial electromagnetic (EM) simulator. In this study,

we utilize FEMTET, which is a 3D-CAE software package by Murata Software Inc. FEMTET implements the finite element method (FEM) and the EM solver can be accelerated by using graphics processing units (GPU). In our image reconstruction algorithm, the procedure of image reconstruction is executed by MATLAB and that of the EM analysis is executed by FEMTET. We can link FEMTET to MATLAB using visual basic (VB) script implemented in Microsoft Excel. The flow chart of the image reconstruction program is shown in **Figure 13**.

5.2.3. Application of S-parameter

In Eq. (6), e^s is the difference between the calculated electric field based on the current complex dielectric constant distribution and the measured electric field at each observation point. Since a vector network analyzer (VNA) is used in the actual measurement, the resulting data are the S parameter. Since S parameters are not directly applicable to Eq. (1), some modifications are required.

On the basis of the reciprocity theorem, the electrical field of the analysis region in the current complex dielectric distribution can be considered as a Green's function $\overline{\mathbf{G}}^b(\mathbf{r}_n|\mathbf{v}_k)$. In FEMTET, it is possible to export electromagnetic fields in a specified region by assuming the input power to the antenna as 1 W. In other words, when $\overline{\mathbf{G}}^b(\mathbf{r}_n|\mathbf{v}_k)$ is given as a field of the analysis region, 1 W can be obtained from the output of the antenna. We consider the image restoration area in a part of the analysis region. While the complex permittivity distribution other than the image reconstruction area is constant, the complex dielectric constant distribution in the image reconstruction area

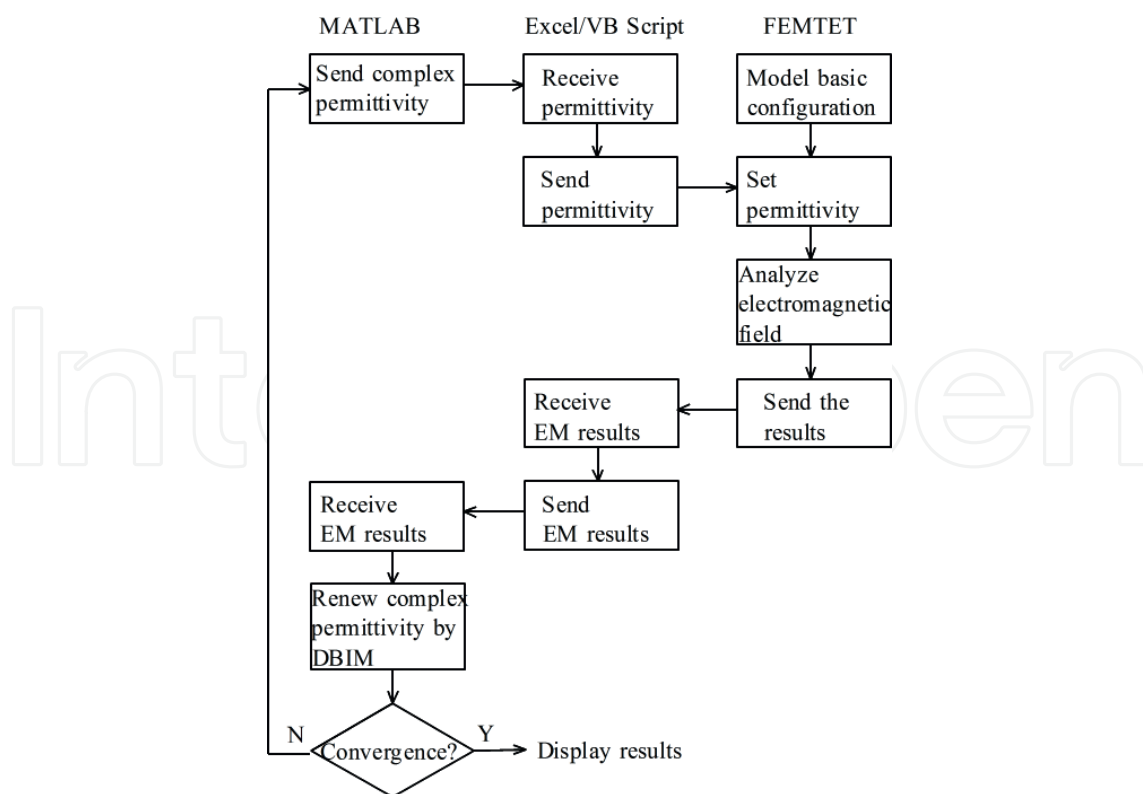


Figure 13. Flowchart of image reconstruction.

is updated. Referring to the structure of the row vector of Eq. (6), the difference between the output power of the antenna before and after the updates can be related to the scattering field on the basis of the change in the complex permittivity distribution of the image restoration area. A sensor including a breast is represented by the multiport circuit network shown in **Figure 14**.

The circuit network equation is expressed using the impedance matrix:

$$\begin{bmatrix} V_1 \\ \vdots \\ V_n \\ \vdots \\ V_N \end{bmatrix} = \begin{bmatrix} Z_{11} & \cdots & Z_{1n} & \cdots & Z_{1N} \\ \vdots & \ddots & \vdots & \ddots & \vdots \\ Z_{n1} & \cdots & Z_{nn} & \cdots & Z_{nN} \\ \vdots & \ddots & \vdots & \ddots & \vdots \\ Z_{N1} & \cdots & Z_{Nn} & \cdots & Z_{NN} \end{bmatrix} \begin{bmatrix} I_1 \\ \vdots \\ I_n \\ \vdots \\ I_N \end{bmatrix} \quad (8)$$

It is assumed that the input and output impedances of the vector network are 50Ω , and that 50Ω loads are connected with the antenna ports other than the measurement antenna. When 1 V is applied to the n th antenna, the current flowing in each load can be expressed as

$$\begin{bmatrix} I_1 \\ \vdots \\ I_n \\ \vdots \\ I_N \end{bmatrix} = \begin{bmatrix} Z_{11} + 50 & \cdots & Z_{1n} & \cdots & Z_{1N} \\ \vdots & \ddots & \vdots & \ddots & \vdots \\ Z_{n1} & \cdots & Z_{nn} + 50 & \cdots & Z_{nN} \\ \vdots & \ddots & \vdots & \ddots & \vdots \\ Z_{N1} & \cdots & Z_{Nn} & \cdots & Z_{NN} + 50 \end{bmatrix}^{-1} \begin{bmatrix} 0 \\ \vdots \\ 1(V) \\ \vdots \\ 0 \end{bmatrix} \quad (9)$$

The received voltage V_n can be calculated using I_n ($n = 1, \dots, N$). Since 1 W is input to the antenna in FEMTET, the AC power supply voltage is 14.14 V. The Z-parameters can be calculated easily from the S-parameters:

$$Z = Z_0 \frac{I + S}{I - S} \quad (10)$$

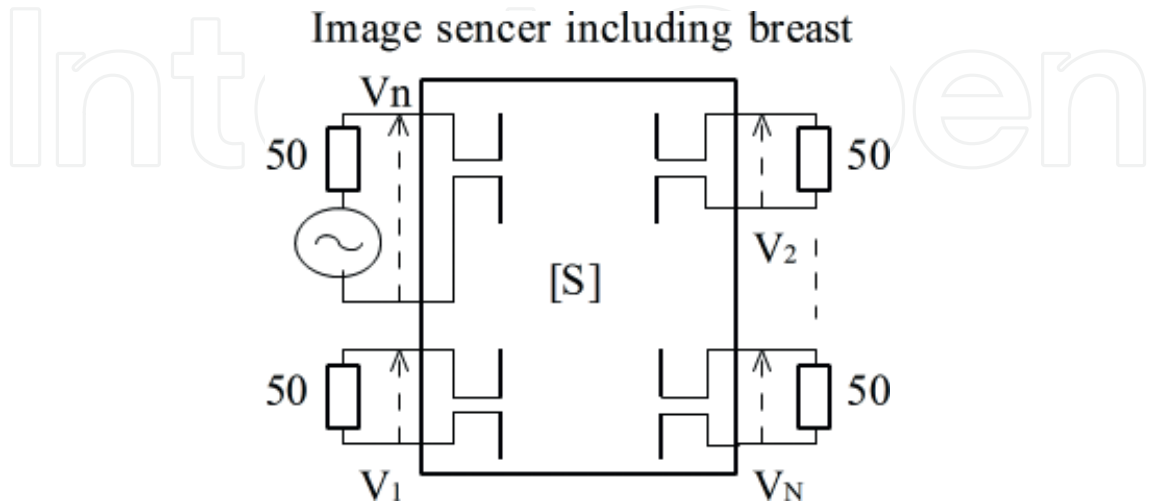


Figure 14. Equivalent circuit of analysis region.

where $Z_0 = 50 \Omega$, and I is the identity matrix. Applying V_n to the left side of Eq. (6), the updated amount of the complex dielectric constant is determined.

5.3. Numerical test

We have developed a numerical phantom as shown in **Figure 15** on the basis of the MRI image of the patient. **Table 2** shows the relative permittivity and conductivity of each tissue at 1.8 GHz. The permittivity and conductivity of the fibroglandular tissues were set at random within the range of values in the table. The phantom is imported to FEMTET, and forward analysis has been carried out at 1.8 GHz. In the image reconstruction, a coarse mesh was used. The breast region is divided into voxels whose side is 12 mm. Three-dimensional images of the set and reconstructed distributions after 100 iterations are shown in **Figure 16**. In order to quantitatively evaluate the image reconstruction, the reconstructed and set values of the permittivity and conductivity with respect to the voxel number are shown in **Figure 17**. The dielectric constant and conductivity are accurately reconstructed.

5.4. Phantom imaging

We have developed a simple microwave tomography shown in **Figure 18** and carried out experiments. It is made of a dielectric block of size $148 \text{ mm} \times 148 \text{ mm} \times 78 \text{ mm}$ with a relative permittivity of 6.2 and conductivity of 0.0367 S/m . Eight dipoles implemented on the dielectric substrate with a relative permittivity of 3.5, $\tan \delta = 0.002$, and a thickness of

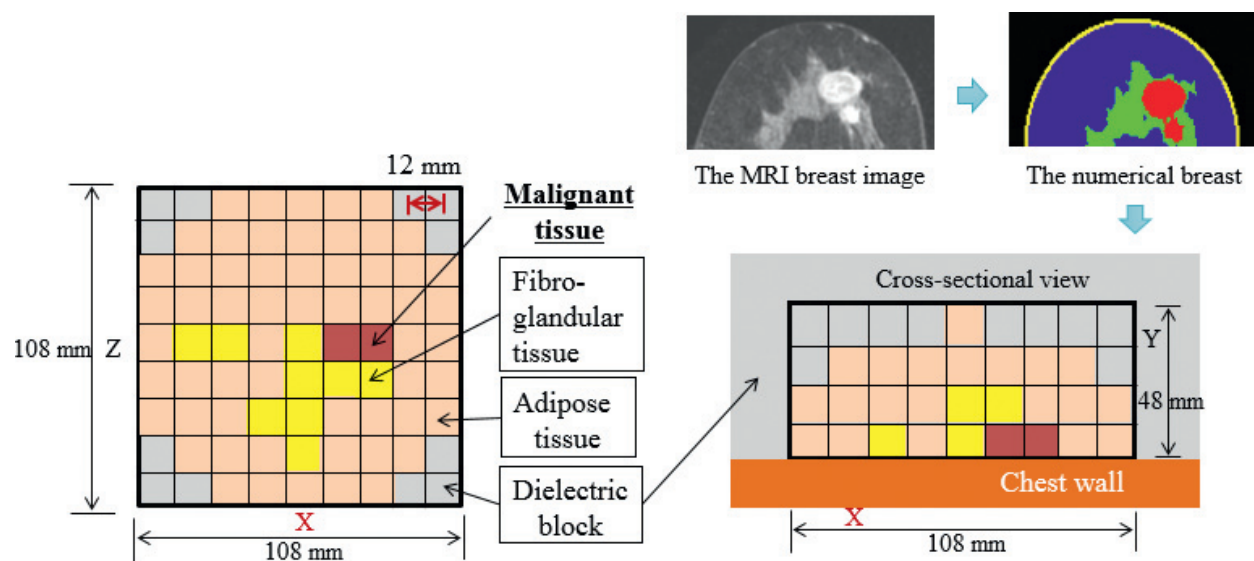


Figure 15. The realistic numerical breast.

| | Malignant tissue | Fibroglandular tissue | Adipose tissue | Dielectric block | Chest wall |
|----------------------------------|------------------|-----------------------|----------------|------------------|------------|
| Relative permittivity ϵ | 52 | 25–35 | 7.0 | 6.2 | 50 |
| Conductivity σ [S/m] | 4.0 | 1.0–2.2 | 0.4 | 0.12 | 2.0 |

Table 2. Relative permittivity and conductivity of each tissue at 1.8 GHz.

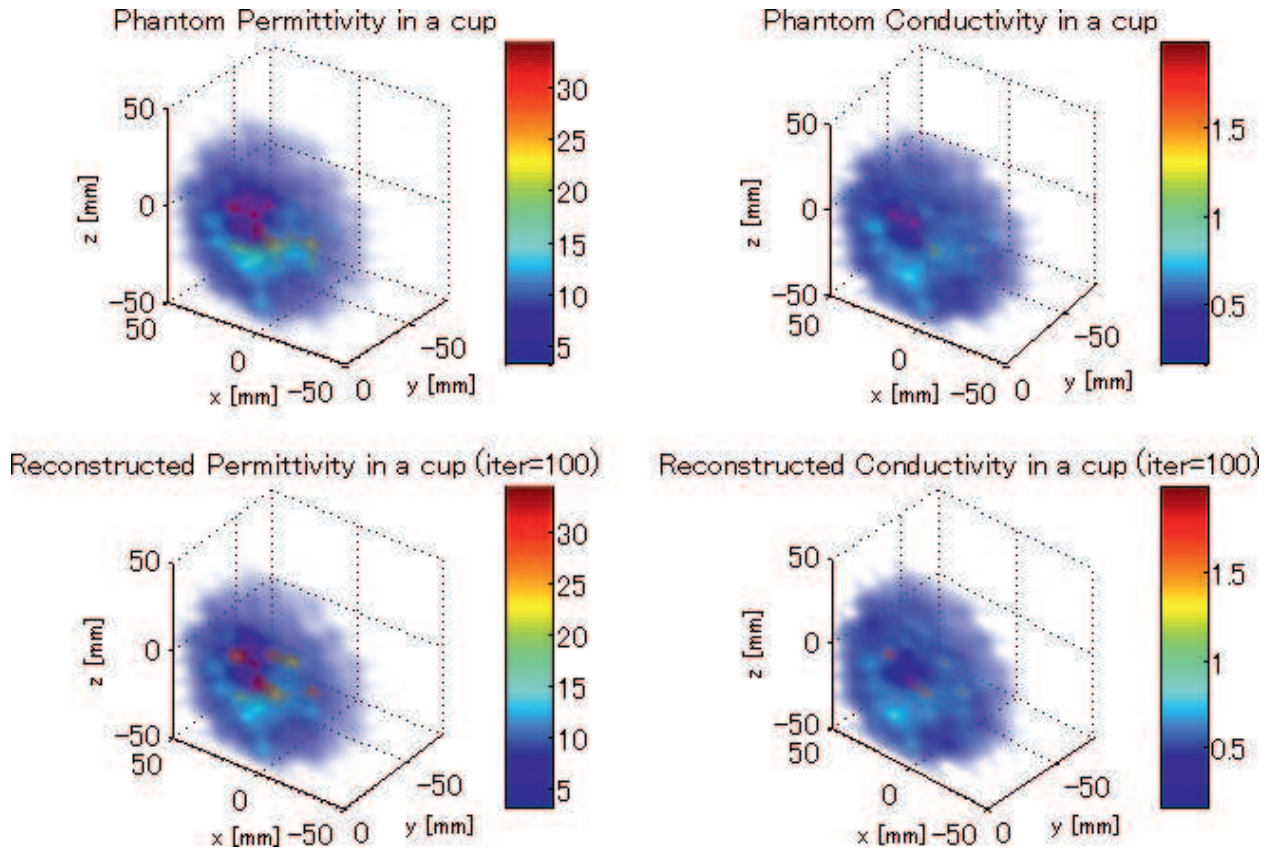


Figure 16. Reconstruction results.

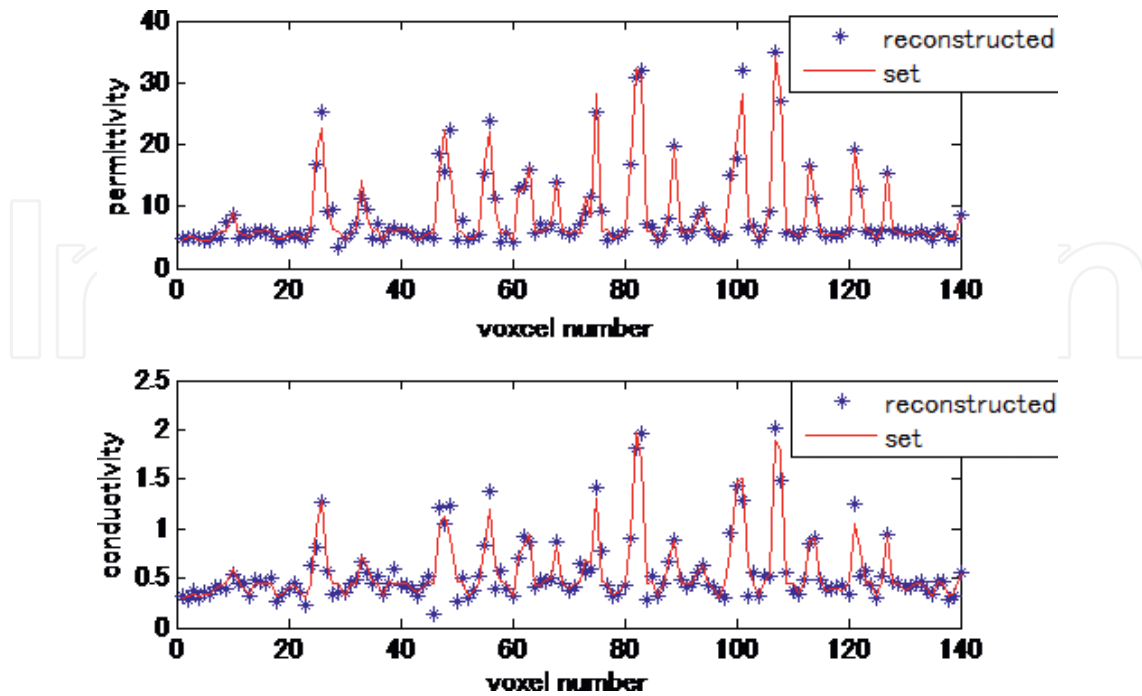


Figure 17. Quantitative evaluation of image reconstruction.

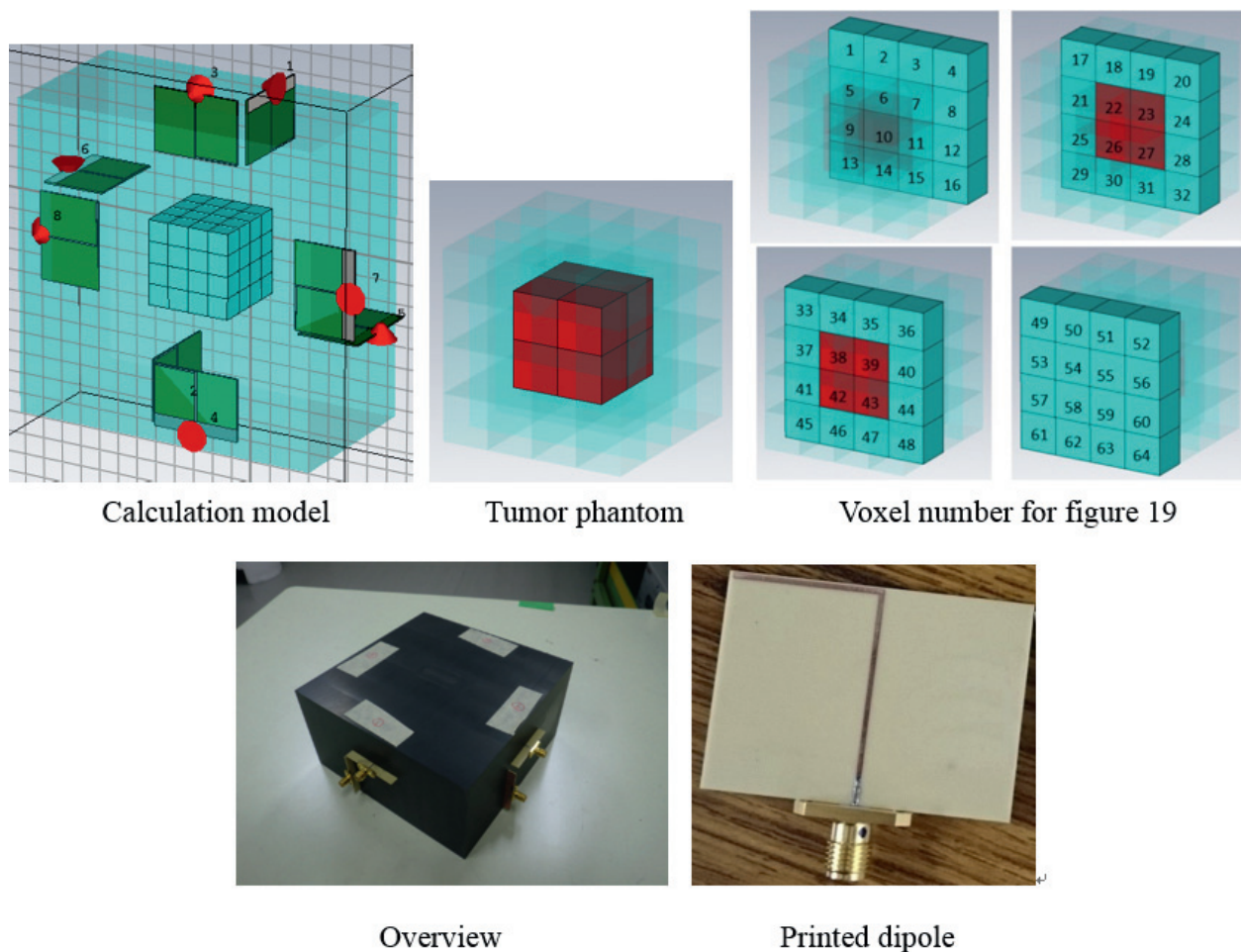


Figure 18. Experiment model.

0.75 mm are inserted into the sidewall. The polarization directions are alternated to allow robust image reconstruction. An imaging region of 40 mm × 40 mm × 40 mm is centered on the dielectric block and is discretized into 64 voxels of 10 mm × 10 mm × 10 mm. Two kinds of models are prepared. One model has an object of size 20 mm × 20 mm × 20 mm, a relative permittivity of 39.4, and conductivity of 0.9994 S/m and is placed at the center of the imaging region. This object simulates a tumor. The other model has no tumor. The measurement frequency is 1.8 GHz. In this model, 8 (monostatic response) + ${}_{8}C_{2}$ (multistatic response) = 36 data points can be obtained. Data correlation between the measured and calculated data is larger than 0.99.

The reconstructed images are shown in **Figure 19**. In order to quantitatively evaluate the reconstructed images, figures that illustrate relative permittivity versus voxel number and three-dimensional images were created. The red line and blue asterisk denote the set relative permittivity and the reconstructed value, respectively. The image is completely reconstructed for a numerical experiment with no modeling and measurement error. However, using the measurement data that includes the modeling and measurement error, the image reconstruction is unsatisfactory regardless of the high data correlation.

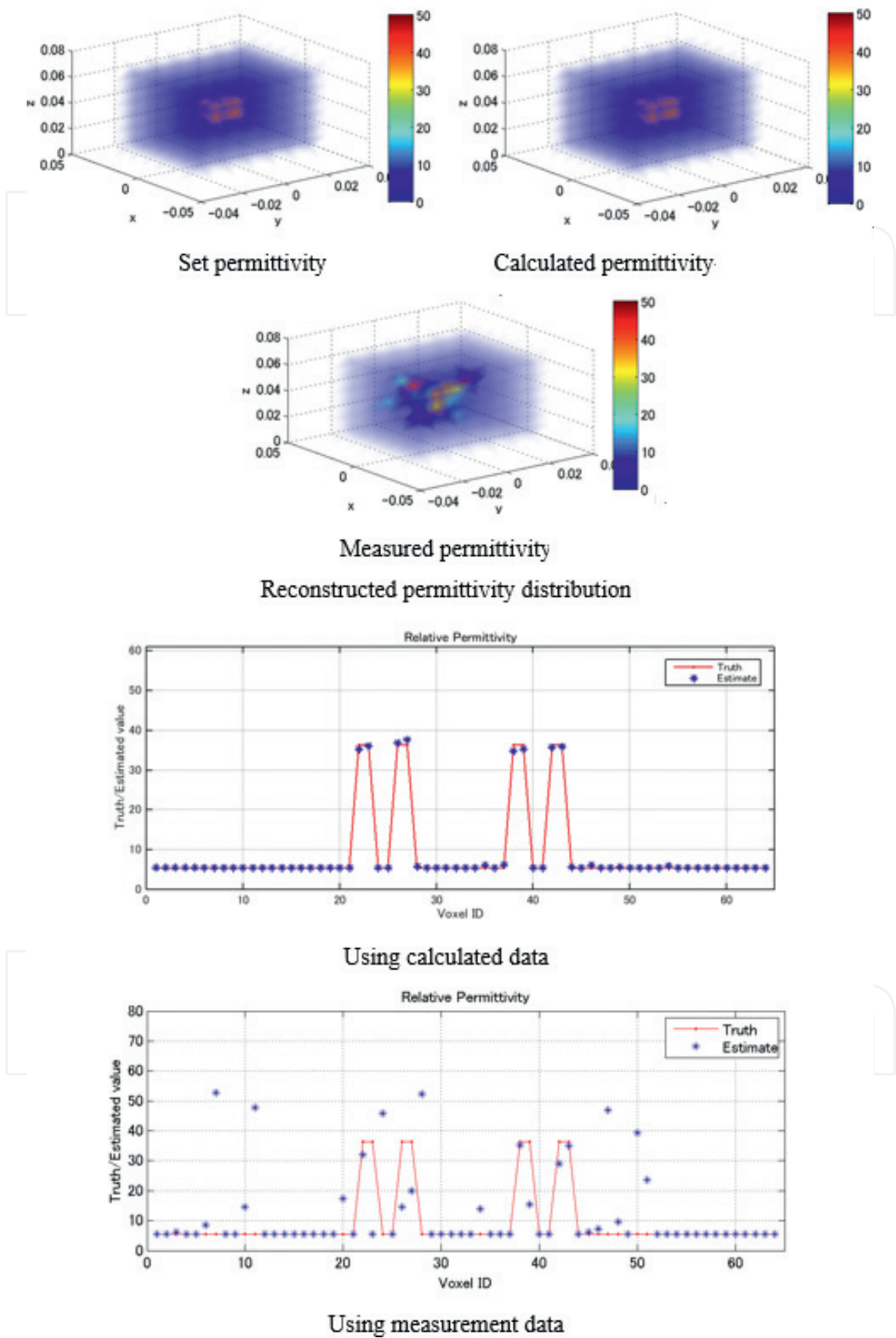


Figure 19. Image reconstruction by conventional method.

5.5. Image reconstruction by radar-assisted microwave tomography

In order to reduce the influence of errors, prior known objective shape and position assumed by the backscattered power distribution provided by the radar instead of a uniform initial distribution is introduced in the inverse scattering problem.

Figure 20 shows the backscattered power distribution using the multistatic adaptive microwave imaging (MAMI) algorithm [18]. The bandwidth is 1–3 GHz. The measured data are used for image reconstruction. The white line indicates the voxels occupied by the object. The height of each sectional view is aligned to the center level of the voxels. The backscattered power strongly corresponds to the object; thus, we can determine the outline of the object. Notably, an ordinary confocal imaging algorithm cannot provide the required image quality.

Figure 21 shows the reconstructed images using the measured data, wherein half the value of the true complex permittivity is set as the objective area. Using prior knowledge, i.e., shape and position of the object, the image can be successfully reconstructed. Although the details cannot be demonstrated owing to the limited space, the images can be reconstructed accurately under the conditions in which there is some disagreement between the scattered power distribution and the position and shape of the object.

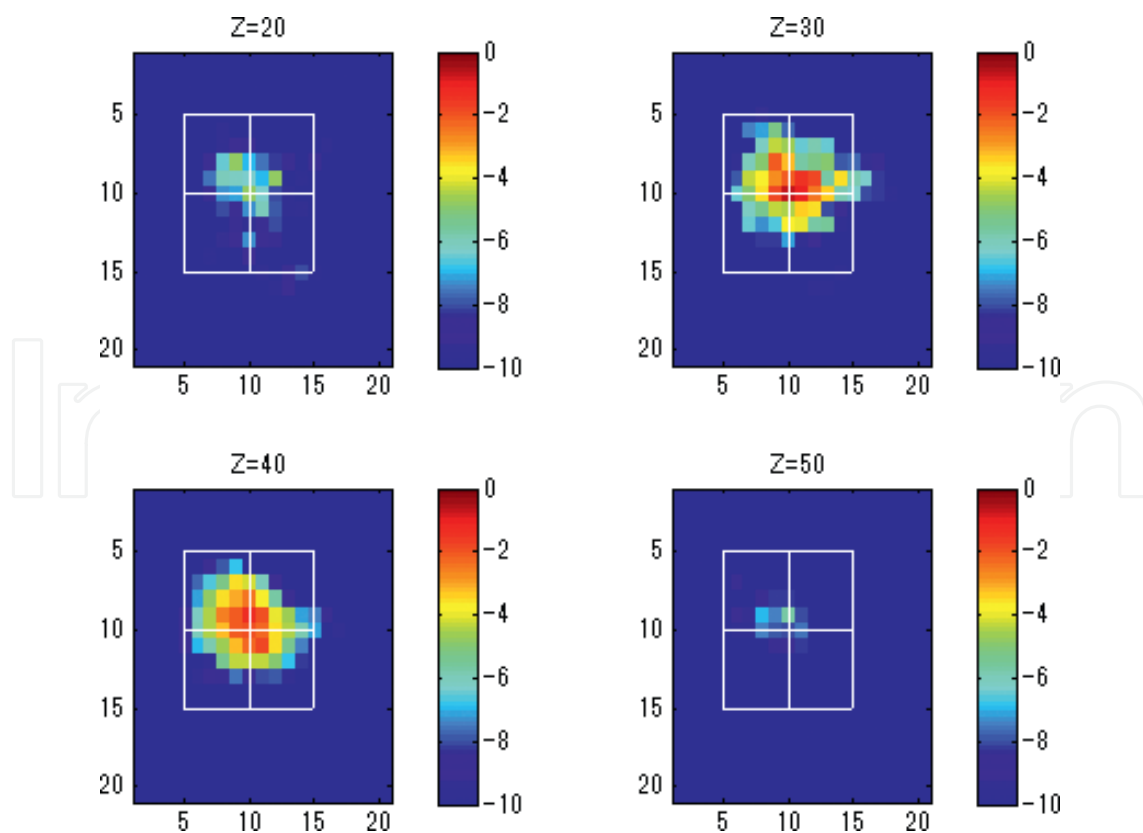


Figure 20. Backscattered power distribution by MAMI.

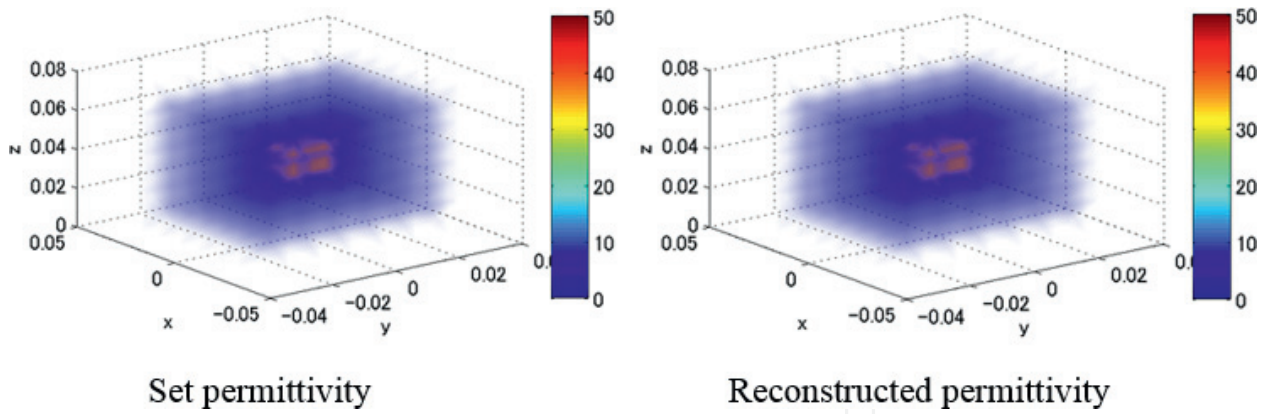


Figure 21. Image reconstruction by the proposed method.

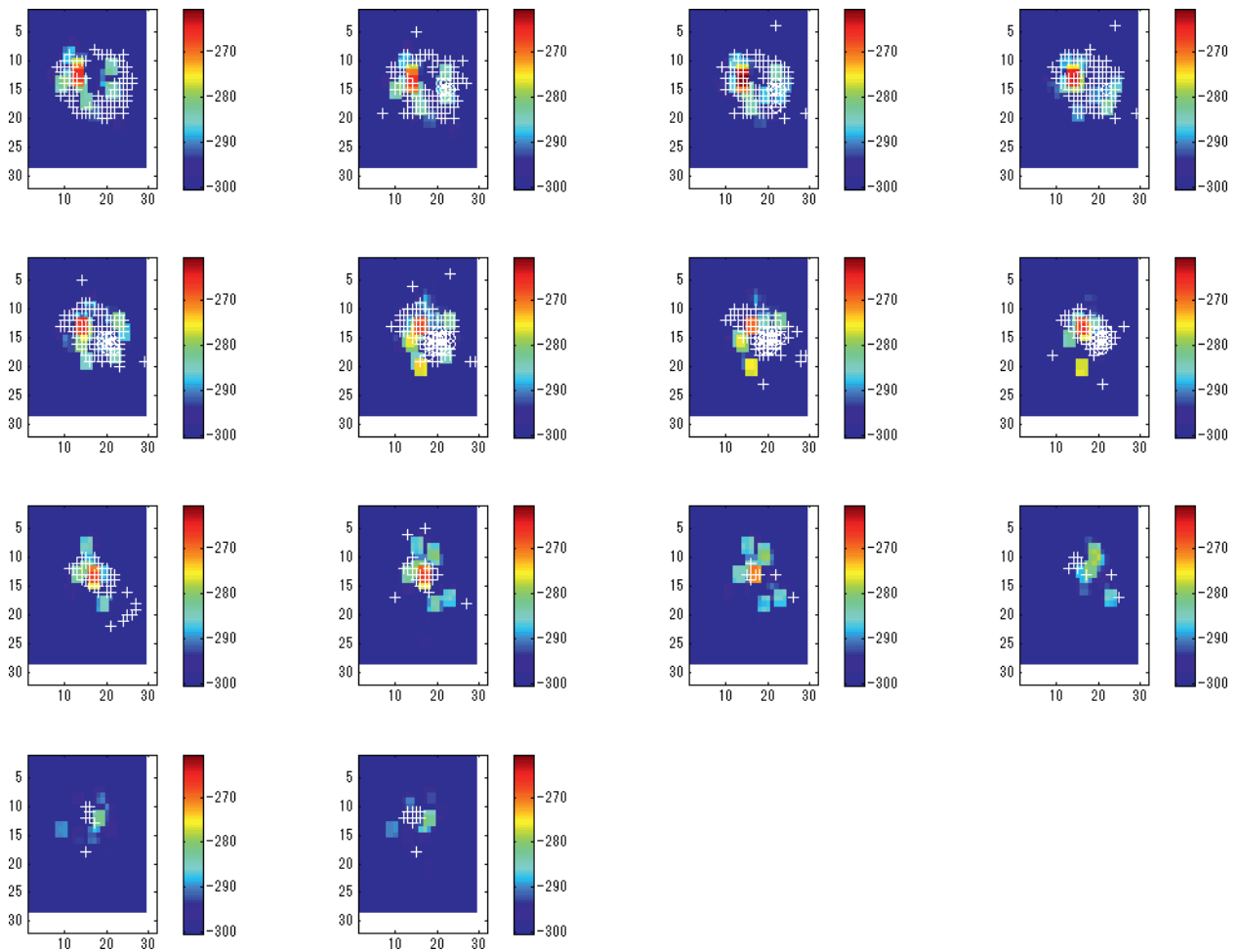


Figure 22. Numerical breast phantom imaging by MAMI.

5.6. Remarks

We have proposed a microwave tomography method using the backscattered power distribution from radar as prior knowledge. It can be confirmed through experiments that the image can be successfully reconstructed under the conditions that modeling and measurement error cannot be ignored.

One might be interested as to whether the method is effective for early breast cancer detection. **Figure 22** shows the backscattered power distribution for a complicated numerical breast phantom. The imaging sensor in **Figure 11** and MAMI were used. The bandwidth is 1–3 GHz. Symbol “+” denotes the positions of the fibroglandular tissue. A strong backscattered signal is generated around the fibroglandular tissue. Therefore, we believe that the proposed technique is effective for early breast cancer detection.

6. Conclusion: key results

Microwave tomography has the potential of a novel modality that can reconstruct both shape and property. However, it is a challenging task to develop equipment using inverse scattering program. Technologies such as sensor with breast fixing by absorption, small sensor with multipolarization, image reconstruction program linking the commercial EM simulator, hybrid imaging method using UWB radar, and inverse scattering are effective ways to aid the development.

It is also necessary to reexamine the use of radar imaging. The glandular structure in the breast is said to have strong symmetry. Using the symmetry, the presence or absence of abnormality can be detected by radar imaging. We are investigating the development of a diagnostic device that detects the presence or absence of abnormality using radar imaging and analyzes the organization properties by tomography with radar information as preliminary knowledge when the abnormality is recognized.

Author details

Yoshihiko Kuwahara

Address all correspondence to: tykuwab@ipc.shizuoka.ac.jp

Shizuoka University, Hamamatsu, Japan

References

- [1] Lehman CD, Isaacs C, Schnall MD, Pisano ED, Accher SM, Weatherall DA, Bluemke DA, Bowen DJ, Marcom PK, Armstrong DK, Domchek SM, Tomlinson G, Skates SJ, Gatsonis C. Cancer yield of mammography, MR, and US in high risk women. *Radiology*. 2007;**224**(2):8. DOI: 10.1148/radiol.2442060461
- [2] Nikolova NK. Microwave imaging for breast cancer. *IEEE Microwave Magazine*. 2011;**12**(7):17. DOI: 10.1109/MMM.2011.942702
- [3] Lazebnik M, McCartney L, Popovic D, Watkins CB, Lindstorm MJ, Harter J, Sewell S, Magliocco A, Brooske JH, Okoniewski M, Hagness SC. A large scale study of the ultra wideband microwave dielectric properties of normal, benign, and malignant breast

- tissues obtained from cancer surgeries. *Physics Medical Biology*. 2007;**52**(20):23. DOI: 10.1088/0031-9155/52/20/002
- [4] Grzegorzczuk TM, Meaney PM, Kaufman PA, diForio-Alexander RM, Paulsen KD. Fast 3D tomographic imaging for breast cancer detection. *IEEE Transaction on Medical Imaging*. 2012;**31**(8):9. DOI: 10.1109/TMI.2012.2197218
- [5] Kuwahara Y, Miura S, Nishina Y, Mukumoto K, Ogura H, Sakahara H. Clinical setup of microwave mammography. *IEICE Transactions on Communications*. 2013;**96**(10):10
- [6] Kuwahara Y, Ogura H, Sakahara H. Development of microwave mammography, consideration of clinical test. In: *Microwave Workshop and Exhibition*; November 28; Yokohama, Japan. IEICE APMC Japan National Committee; 2013. 4 p
- [7] Kuwahara Y, Suzuki K, Horie H. Conformal array antenna with aspirator for microwave mammography. In: *IEEE International Symposium on Antennas and Propagation*, July 13, Toronto. IEEE; 2010. p. 234.11. DOI: 10.1109/APS.2010.5561879
- [8] Mohamed L, Kuwahara Y. Study of correlation coefficient for breast tumor detection in microwave tomography. *Open Journal Antennas and Propagation*. 2015;**3**(4):10. DOI: 10.4236/ojapr.2015.34004
- [9] Kuwahara Y. Microwave mammography with a small sensor and a commercial electromagnetic simulator. In: *European Microwave Conference*, October 6, London; 2016. 4 p. DOI: 10.1109/EuMC.2016.7824430
- [10] Kuwahara Y. Application of S parameter to the inverse scattering problem. In: *European Conference on Antennas and Propagation*, March 21, Paris; 2017. 4 p
- [11] Ono Y, Kuwahara Y. Microwave tomography assisted by radar imaging. In: *European Microwave Conference*; October, Nurnberg; 2017. 4 p
- [12] Shea JD, Kosmas P, Hagness SC, VanVeen BD. Three dimensional microwave imaging of realistic numerical breast phantoms via a multiple frequency inverse scattering technique. *Medical Physics*. 2010;**37**(8):17. DOI: 10.1118/1.3443569
- [13] Mays RO, Behdad N, Hagness SC. A TSVD analysis of the impact of polarization on microwave breast imaging using an enclosed array of miniaturized patch antennas. *IEEE Antennas and Wireless Propagation Letters*. 2015;**14**:4. DOI: 10.1109/LAWP.2014.2365755
- [14] Gabriel C, Gabriel S, Corthout E. The dielectric properties of biological tissues: 1. Literature survey. *Physics Medical Biology*. 1996;**41**:19
- [15] Sadiku MNO, editors. *Numerical Techniques in Electromagnetics with MATLAB*. New York: CRC Press; 2009. 710 p
- [16] Bond EJ, VanVeen BD, Hagness SC. Microwave imaging via space time beamforming for early detect of breast cancer. *IEEE Transactions on Antennas and Propagation*. 2003;**51**(8):16. DOI: 10.1109/TAP.2003.815446

- [17] Klemm M, Creddock IJ, Leenderts JA, Preece A, Gibbins DR, Share M, Benjami R. Clinical trials of a UWB imaging radar for breast cancer. In: European Conference on Antennas and Propagation, 12–16 April, Barcelona, IEEE; 2010. p. 4
- [18] Xie Y, Guo B, Xu L, Li J, Stocia P. Multiple adaptive microwave imaging for early breast cancer detection. IEEE Transaction on Biomedical Engineering. 2006;**53**(8):11. DOI: 10.1109/ICASSP.2006.1660407

IntechOpen

IntechOpen

